

# Hydrogen-Induced Disproportionation of Samarium-Cobalt Intermetallics Enabling Promoted Hydrogen Evolution Reaction Activity and Durability in Alkaline Media

Ziliang Chen,\* Stefan Mebs, Indranil Mondal, Hongyuan Yang, Holger Dau, Zhenhui Kang,\* Michael Haumann, Suptish Ghosh, Wanglai Cen, Matthias Driess, and Prashanth W. Menezes\*

Transition-metal nanoparticles hold great promise as electrocatalysts for alkaline hydrogen evolution reaction (HER), however, addressing the simultaneous challenges of ensuring sufficient active sites, promoting favorable water dissociation, and optimizing binding energy toward hydrogen intermediates remains a formidable task. To overcome these hurdles, a novel gaseous hydrogen engineering strategy is proposed by in situ embedding cobalt nanoparticles within a samarium hydride matrix (Co/SmH<sub>2</sub>) via hydrogen-induced disproportionation of SmCo<sub>5</sub> particles for efficient alkaline HER. The as-designed Co/SmH<sub>2</sub> delivered an overpotential as low as 252 mV at 100 mA cm<sup>-2</sup>, surpassing the performance of pristine Co by 100 mV. Notably, this catalyst lasts remarkably long maintaining a durability at ≈500 mA cm<sup>-2</sup> for 120 h. A combination of in situ Raman spectroscopy, in situ X-ray absorption spectroscopy, density functional theory calculation and post-HER characterizations unambiguously unveiled that the surface SmH<sub>2</sub> transforms into samarium (hydr)oxide during electrocatalysis. This transformation not only inhibits the aggregation of the ultrafine cobalt nanoparticles but also significantly enhances the water dissociation and optimizes the binding energy of active cobalt species toward hydrogen intermediate, resulting in concurrent improvement of kinetics, thermodynamics, and stability of the HER process.

## 1. Introduction

Hydrogen is widely regarded as the optimal energy carrier owing to its clean and renewable nature. Water electrolysis is one of the most eco-friendly, green, and sustainable methods to produce hydrogen fuel.<sup>[1]</sup> However, the hydrogen evolution reaction (HER), a crucial half-reaction in water electrolysis, suffers from sluggish kinetics and is thermodynamically uphill.<sup>[2,3]</sup> Typically, noble metal-based electrocatalysts, such as Pt, are usually required to be incorporated for HER to reduce the energy barrier.<sup>[4]</sup> Unfortunately, the limited resources and high cost of Pt-based electrocatalysts present significant obstacles to their widespread adoption.<sup>[5]</sup> Within this context, developing electrocatalysts that offer both cost-effectiveness and high efficiency is of great interest for practical HER applications. On the other hand, it is generally accepted that an acidic medium is conducive to the HER, given its proton-rich environment that facilitates hydrogen adsorption

Z. Chen, Z. Kang  
Institute of Functional Nano & Soft Materials (FUNSOM), Jiangsu Key  
Laboratory for Carbon-Based Functional Materials & Devices  
Soochow University  
199 Ren'ai Road, Suzhou, Jiangsu 215123, P. R. China  
E-mail: zlchen@suda.edu.cn; zhkang@suda.edu.cn

Z. Chen, P. W. Menezes  
Material Chemistry Group for Thin Film Catalysis–CatLab  
Helmholtz-Zentrum Berlin für Materialien und Energie  
Albert-Einstein-Str. 15, 12489 Berlin, Germany  
E-mail: prashanth.menezes@mailbox.tu-berlin.de

 The ORCID identification number(s) for the author(s) of this article can be found under <https://doi.org/10.1002/adfm.202402699>

© 2024 The Authors. Advanced Functional Materials published by Wiley-VCH GmbH. This is an open access article under the terms of the [Creative Commons Attribution](#) License, which permits use, distribution and reproduction in any medium, provided the original work is properly cited.

DOI: 10.1002/adfm.202402699

S. Mebs, H. Dau, M. Haumann  
Fachbereich Physik  
Freie Universität Berlin  
Arnimallee 14, 14195 Berlin, Germany

I. Mondal, H. Yang, S. Ghosh, M. Driess, P. W. Menezes  
Department of Chemistry: Metalorganics and Inorganic Materials  
Technische Universität Berlin  
Straße des 17 Juni 135, Sekr. C2, 10623 Berlin, Germany

W. Cen  
Institute of New Energy and Low Carbon Technology  
Sichuan University  
Chengdu 610065, P. R. China

on the catalyst surface.<sup>[6]</sup> However, the corrosive acidic fog generated by the acidic electrolyte would inevitably cause severe chemical corrosion of electrolyzers and contamination of the produced hydrogen gas.<sup>[7,8]</sup> Consequently, significant attention has shifted toward alkaline HER, where the alkaline electrolyte bears the lower vapor pressure and relatively milder chemical environment.<sup>[9–11]</sup> More importantly, non-platinum group metals, specifically Fe, Co, and Ni, exhibit significant promise as electrocatalysts for alkaline HER, owing to their cost-effectiveness, abundant availability, and high conductivity.<sup>[12–19]</sup> Despite these advantages, these transition-metal(s) still fall short in the alkaline HER environment compared to the electrocatalytic activity achieved by Pt. This is because they bear a strong adsorption ability toward hydrogen intermediate and lack effective water dissociation sites for the sluggish Volmer step of alkaline HER (i.e., breaking of the strong H–OH bond).<sup>[7,20–22]</sup> Moreover, these pristine metals are susceptible to deactivation in the longer run due to the coverage or etching of active sites by hydroxyl groups.<sup>[9]</sup> Therefore, it is highly desired to seek a strategy that can effectively increase the number of active sites and water dissociation sites as well as essentially optimize the adsorption free energy of transition-metals toward hydrogen intermediate in alkaline HER.

Recent studies have confirmed that synergistic coupling of oxophilic compounds with metal electrocatalysts is a viable strategy to boost their alkaline HER catalytic performance.<sup>[23–32]</sup> Specifically, oxophilic compounds usually exhibit a strong capability to cleave the H–OH bonds in water molecules, thus accelerating the Volmer step of alkaline HER and alleviating the coverage of (hydr)oxide ligands onto active sites.<sup>[23,24]</sup> For example, Ni/NiO,<sup>[25]</sup> Ni/Ni(OH)<sub>2</sub>,<sup>[26]</sup> Co(OH)<sub>2</sub>/MoS<sub>2</sub>,<sup>[27]</sup> Pt/(Fe,Ni)(OH)<sub>2</sub>,<sup>[28]</sup> Pt/Ni(OH)<sub>2</sub>,<sup>[29]</sup> and Ru/Ni(OH)<sub>2</sub><sup>[30]</sup> electrocatalysts have been successively designed and prepared for alkaline HER in recent years, marking significant progress. However, a notable challenge arises as these coupled transition-metal (hydr)oxides are prone to reduction into metals at high potentials due to their low thermodynamic stability, resulting in poor cycling stability.<sup>[32]</sup> Compared to these transition metal (hydr)oxides, rare earth metal (hydr)oxides possess superior oxophilicity and thermodynamic stability, rendering them a promising class of promoters for water dissociation.<sup>[32–34]</sup> On the basis of these premises, the combination of rare earth hydroxides with transition-metals holds the potential for enhancing stability, yet this avenue of investigation remains underexplored. Furthermore, the challenge persists in developing a single, controllable approach to effectively couple rare earth (hydr)oxides with transition metal nanoparticles in a well-defined manner.

More recently, we introduced an innovative gaseous hydrogen engineering strategy that utilizes hydrogen-induced lattice strain of LaNi<sub>5</sub> precatalyst under ambient conditions.<sup>[35]</sup> This approach effectively pulverizes particles, exposes metal sites, and accelerates reconstruction during oxygen evolution reactions, resulting in enhanced catalytic performance. Remarkably, elevating the reaction temperature for hydrogenation to the critical point may induce the hydrogen atoms residing in the interstitials of rare earth-transition-metal intermetallic hydrides to trigger phase decomposition. This process leads to the formation of rare earth metal hydrides and transition-metal phases.<sup>[36,37]</sup> Furthermore, in accordance with the Pourbaix phase diagram, it is anticipated

that the surface of rare earth hydrides will eventually convert into the corresponding rare earth (hydr)oxides under alkaline HER conditions.<sup>[38]</sup> From these aspects, it becomes evident that gaseous hydrogen engineering holds promise as a feasible approach to in situ construct a well-defined composite composed of rare earth (hydr)oxides and transition-metals. However, the microstructure of the products resulting from gaseous hydrogen-induced phase decomposition remains elusive.

Inspired by the aforementioned considerations, we utilized gaseous hydrogen to induce the disproportionation of SmCo<sub>5</sub> intermetallic for catalyzing HER. The selection of SmCo<sub>5</sub> as our model is based on its commercial availability and demonstrated capability to store hydrogen within its interstitials.<sup>[39,40]</sup> Furthermore, if SmH<sub>2</sub> is formed by hydrogenation, it is expected to be converted into samarium hydr(oxide) under the harsh alkaline HER condition in accordance with the Pourbaix diagram.<sup>[38]</sup> Thus, this contribution seeks to address the following research questions: i) what are the microstructural features of gaseous hydrogen-treated SmCo<sub>5</sub>? ii) how does gaseous hydrogen-treated SmCo<sub>5</sub> perform in alkaline HER? iii) what is the phase evolution of gaseous hydrogen-treated SmCo<sub>5</sub> during HER? And iv) if Sm species undergo changes during alkaline HER, whether and/or how does the newly formed phase influence the HER performance? To answer these questions, herein, a series of in situ and ex situ spectroscopic experiments along with theoretical calculations have been performed. Our investigation reveals a complete phase transformation from SmCo<sub>5</sub> to SmH<sub>2</sub> and Co after hydrogenation at 500 °C under 5 MPa H<sub>2</sub>, in which Co nanocrystals are uniformly confined by SmH<sub>2</sub> nanocrystals. Subsequently, during alkaline HER, a surface reconstruction of SmH<sub>2</sub>/Co particle takes place wherein SmH<sub>2</sub> transforms into samarium (hydr)oxide, continuing to uniformly constrain Co nanocrystals. As anticipated, Sm(OH)<sub>3</sub> greatly optimizes the binding energy of Co to H, promotes water dissociation, and stabilizes the structure of the material. Consequently, the as-prepared precatalyst deposited on nickel foam (NF) shows an excellent HER performance with an overpotential as low as 252 mV at 100 mA cm<sup>-2</sup> and long durability for 120 h at ~500 mA cm<sup>-2</sup>, surpassing the performance of pristine cobalt nanoparticles.

## 2. Results and Discussion

The phase transformation from SmCo<sub>5</sub> to SmH<sub>2</sub> and Co via gaseous hydrogen treatment was schematically illustrated in **Figure 1a**. Specifically, upon the hydrogenation under 5 MPa at 500 °C, hydrogen atoms initially diffuse along the grain boundaries of the SmCo<sub>5</sub> crystallites and partially induce the phase disproportionation, resulting in the formation of SmH<sub>2</sub> and Co nanocrystals. With extended hydrogenation time, a complete phase conversion from SmCo<sub>5</sub> to SmH<sub>2</sub> and Co occurs. Interestingly, these Co nanocrystals were homogeneously confined within SmH<sub>2</sub> nanocrystals. The phase transformation was first demonstrated by X-ray diffraction (XRD) patterns. **Figure S1** (Supporting Information) illustrates the dependence of phase components on hydrogenation time, revealing an increase of the phase transformation against hydrogenation time, and a complete transformation could be achieved by 24 h of hydrogenation. To better understand the phase structure before and after phase disproportionation, the Rietveld refinement was performed for

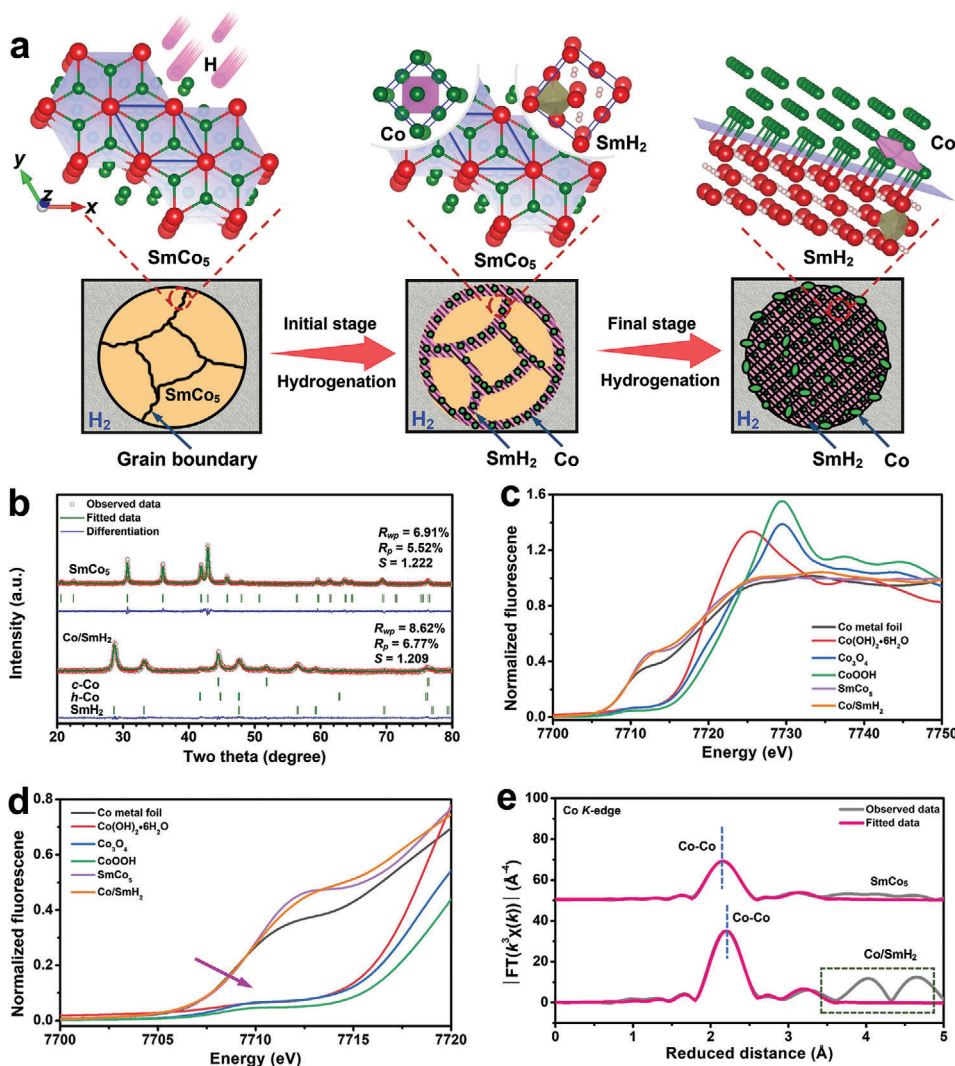


**Figure 1.** a) Schematic illustration for the hydrogen-induced phase disproportionation of  $\text{SmCo}_5$  compound. b) Rietveld refinement for the XRD patterns of  $\text{SmCo}_5$  compound before (top traces) and after (bottom traces) hydrogenation (red dots, experimental data; green lines, simulations), “difference” denotes the difference between the experimental and simulated spectra; c) XANES spectra for the  $\text{SmCo}_5$  compound before and after hydrogenation, together with several cobalt reference compounds; d) Magnification of the pre-edge region of the XANES spectra; e) Fourier-transforms of EXAFS spectra at the Co K-edge in the  $\text{SmCo}_5$  compound before (top traces) and after (bottom traces) hydrogenation (green lines, experimental data; red lines, simulations). For the corresponding EXAFS fit parameters, see Table S3 (Supporting Information).

the XRD patterns of the  $\text{SmCo}_5$  compound and the gaseous hydrogen-treated  $\text{SmCo}_5$  compound after 24 h. As shown in Figure 1b and Table S1 (Supporting Information), the  $\text{SmCo}_5$  compound exhibited a pure hexagonal crystalline phase before hydrogenation, while after 24 h of hydrogenation, this phase disappeared, and a mixture of new  $\text{SmH}_2$  and  $\text{Co}$  phases was observed. Moreover, the phase abundance for  $\text{SmH}_2$  and  $\text{Co}$  phases were 37 and 63 wt.%, respectively, which was quite close to the theoretical value and inductively coupled plasma atomic emission spectrometry (ICP-OES) results (Table S2, Supporting Information), i.e., the molar ratio of  $\text{Co}$  to  $\text{Sm}$  is 1:5. Note that the  $\text{Co}$  phase predominantly crystallizes in a cubic crystal structure accompanied with minor hexagonal crystal structure. The X-ray absorption near edge structure (XANES) in X-ray absorption spectra (XAS) at the Co K-edge further demonstrated the metallic state

of  $\text{Co}$  species in as-prepared  $\text{SmCo}_5$  and hydrogenated  $\text{SmCo}_5$  (Figure 1c,d). In addition, the corresponding extended X-ray absorption fine structure (EXAFS) spectra showed that besides the shortest  $\text{Co-Co}$  distances in  $\text{SmCo}_5$  and  $\text{Co}$  metal, two Fourier-transform peak features (at ca. 4.3 and 4.75 Å) gain intensity in the spectrum denoted  $\text{Co/SmH}_2$ . These features are assigned to  $\text{Co-Co}$  distances in the metallic  $\text{Co}$  phase (Figure 1e; Figures S2 and S3 and Table S3, Supporting Information), consistent with previous reports.<sup>[41,42]</sup> Meanwhile, the XANES and EXAFS spectra of  $\text{Sm L}_3$ -edge also demonstrated  $\text{SmH}_2$  to be the dominating species after the hydrogenation of  $\text{SmCo}_5$  (Figures S4 and S5 and Table S4, Supporting Information). Note that very weak signals for the  $\text{Sm-Co}$  bond could also be identified, which might be assigned to the formation of abundant heterointerfaces between nanosized  $\text{Co}$  and  $\text{SmH}_2$ . The above findings confirmed again

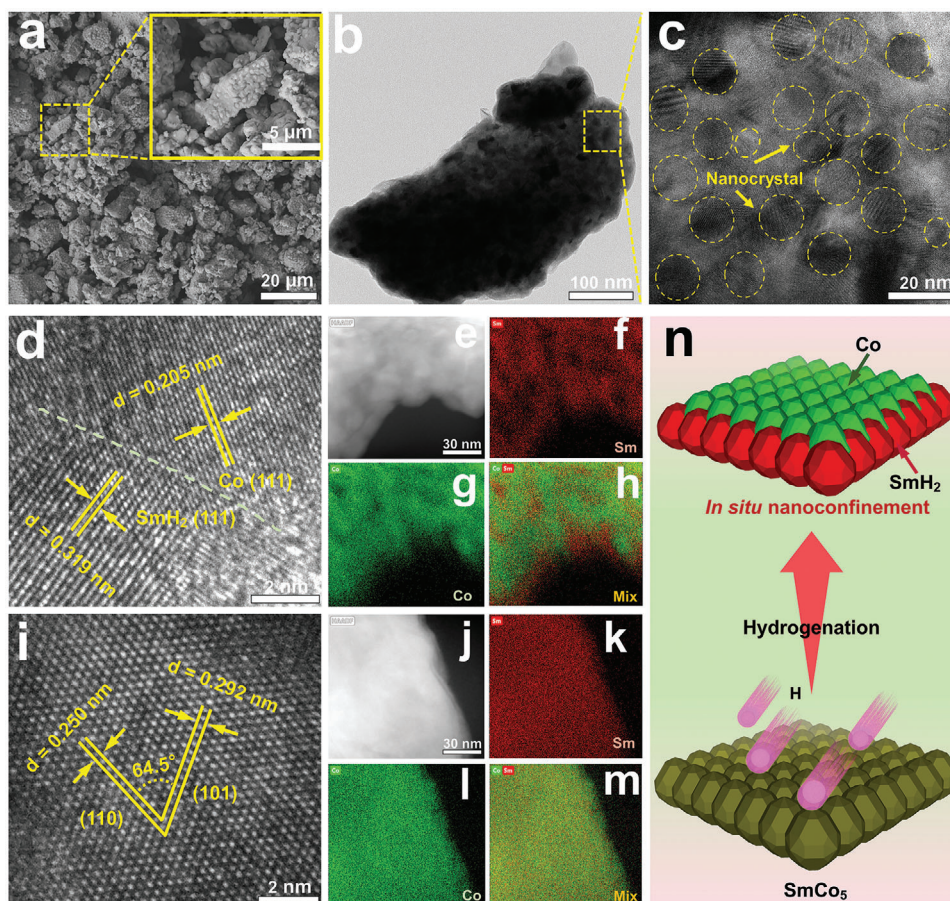


**Figure 2.** a) FESEM image of representative FTO-supported Co/SmH<sub>2</sub> particle, b) TEM image, c) magnified and d) high-resolution (HR)TEM images, and e) the HAADF image of representative Co/SmH<sub>2</sub> particle scratched from FTO as well as the corresponding EDX elemental mapping of f) Sm, g) Co, and h) their mixture. i) high-resolution (HR)TEM image and j) the HAADF image of representative SmCo<sub>5</sub> particle as well as the corresponding EDX elemental mapping of k) Sm, l) Co, and m) their mixture. n) Schematic illustration for the hydrogen-induced formation of heterophases composed of Co and SmH<sub>2</sub>.

the transformation of the SmCo<sub>5</sub> phase into the Co and SmH<sub>2</sub> phases.

The surface chemical information of samples was assessed through X-ray photoelectron spectroscopy (XPS) spectra, and the results are presented in Figure S6 (Supporting Information). As shown in Figure S6a,b (Supporting Information), in addition to the signals for metallic Co, both Co<sup>n+</sup> and Sm<sup>3+</sup> were also observed in the high-resolution Co 2p and Sm 3d XPS spectra of the SmCo<sub>5</sub> compound. This phenomenon, common for transition metals and alloys, is attributed to the presence of a passivation layer.<sup>[36,43–45]</sup> After hydrogenation, the signals for these elemental species were very similar (Figure S6, Supporting Information). The presence of Co<sup>n+</sup> and Sm<sup>3+</sup> may also result from oxygen adsorption on the surface of fresh Co and SmH<sub>2</sub> upon exposure to air.

To examine the evolution of morphology and microstructure, we made a comparative analysis of field emission scanning electron microscopy (FESEM) results for the SmCo<sub>5</sub> particles before and after hydrogenation. As depicted in Figure S7 (Supporting Information), the original SmCo<sub>5</sub> compound exhibited an irregular pseudo-spherical shape with sizes ranging from 200 nm to

20 μm, presenting a smooth surface. Although the particle size of the hydrogenated SmCo<sub>5</sub> was largely conserved, the particles displayed a markedly roughened surface with a distinctive wrinkled sheet morphology (Figure S7, Supporting Information), indicating discernible surface alterations induced by gaseous hydrogen treatment. As we had considered evaluating the catalytic alkaline HER onto conductive fluorine-doped tin oxide glass (FTO) substrate, we further deposited the Co/SmH<sub>2</sub> powder onto a conductive FTO glass matrix (Co/SmH<sub>2</sub>@FTO), which revealed that the Co/SmH<sub>2</sub> particles retained the same morphology as the pristine compound (Figure 2a). In line with the FESEM results, the low-magnification transmission electron microscope (TEM) image of powder scratched from the FTO exhibited the identical morphology of the hydrogenated SmCo<sub>5</sub> particles (Figure 2b). Besides, the selected area electron diffraction (SAED) pattern confirmed the coexistence of the Co and SmH<sub>2</sub> phases (Figure S8, Supporting Information). Interestingly, the magnified TEM image demonstrated that the particle was composed of numerous nanocrystals (Figure 2c). A further high-resolution TEM (HRTEM) image proved the formation of heterophases, in which the Co phase was uniformly confined by the SmH<sub>2</sub> phase. In particular, the

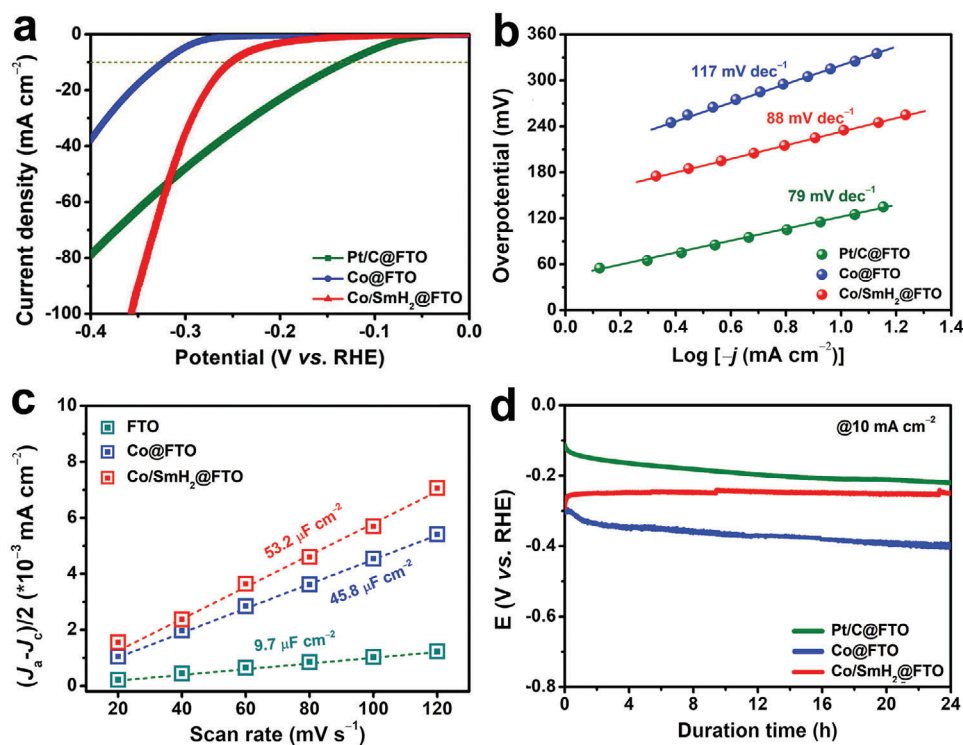


**Figure 3.** a) LSV curves of Co, Co/SmH<sub>2</sub>, and Pt/C on FTO recorded at a scan rate of 5 mV s<sup>-1</sup>. Comparison of b) Tafel slope by steady state method, c) C<sub>dl</sub> values of Co@FTO, Co/SmH<sub>2</sub>@FTO, and FTO, and d) chronopotentiometry curve for Pt/C, Co and Co/SmH<sub>2</sub> on FTO.

lattice distances of 0.205 and 0.319 nm corresponded to the (111) facet of the cubic Co phase and the (111) facet of the cubic SmH<sub>2</sub> phase, respectively (Figure 2d, additional TEM images in Figure S9, Supporting Information). To demonstrate this confinement, high-angle angular dark field-scanning transmission electron microscopy (HAADF-STEM) images and corresponding elemental mappings are provided in Figure 2e–h. Evidently, the signals for Co and Sm elements were uneven, showcasing the uniform confinement of Co species by Sm species. This was also supported by the HAADF-STEM and corresponding elemental mappings with a high magnification for an entire particle (Figure S10, Supporting Information). In stark contrast, the pristine SmCo<sub>5</sub> compound only exhibited the pure hexagonal SmCo<sub>5</sub> phase when compared to the hydrogenated SmCo<sub>5</sub> compound. As presented in Figure 2i, lattice distances of 0.250 and 0.292 nm corresponded to the (110) and (101) facets of the SmCo<sub>5</sub> phase, generating an intersection angle of ≈65° (more TEM images are shown in Figure S11, Supporting Information). HAADF-STEM images and corresponding elemental mappings vividly displayed the overlap of Sm and Co species (Figure 2j–m). Overall, the above results confirmed that the hydrogen-induced disproportionation strategy effectively achieves in situ homogeneous confinement of rare earth metal hydrides toward transition metal nanocrystals (Figure 2n), potentially triggering unexpected catalytic performance.

To probe the catalytic activity toward alkaline HER, the as-prepared Co/SmH<sub>2</sub> powder was deposited onto FTO (Co/SmH<sub>2</sub>@FTO), which was then served as a working electrode in 1.0 M KOH. For comparison, the catalytic activity of pristine Co particles with an average size of 2 μm and commercial Pt/C deposited onto FTO with the same mass

loading were also examined under identical conditions (Figure S12, Supporting Information). As shown in Figure 3a, the overpotential of Co/SmH<sub>2</sub>@FTO at 10 mA cm<sup>-2</sup> was 251 mV, which was far lower than that (326 mV) of Co@FTO. This result strongly suggested the significant improvement of HER activity for Co achieved through the strategic confinement of SmH<sub>2</sub>. While slightly lower in activity than the commercial Pt/C@FTO (150 mV), the Tafel slope of Co/SmH<sub>2</sub>@FTO (88 mV dec<sup>-1</sup>) is much lower than that of Co@FTO (117 mV dec<sup>-1</sup>), which is also close to that of Pt/C@FTO (79 mV dec<sup>-1</sup>). This observation implies that the presence of SmH<sub>2</sub> effectively enhances the reaction kinetics of HER. This result could also be validated by the electrochemical impedance spectrum (EIS) (Figure S13, Supporting Information), where Co/SmH<sub>2</sub>@FTO exhibited a significantly lower charge transfer resistance (11 Ω) compared to Co@FTO (37 Ω). C<sub>dl</sub> values of bare FTO, Co/SmH<sub>2</sub>@FTO, and Co@FTO derived from CV curves at potential scan rates from 20 to 120 mV s<sup>-1</sup> (Figure S14, Supporting Information) are also shown and compared in Figure 3c, which indicated the close number of potential active sites for catalysis. This result also implied the more favorable catalytic activity of Co/SmH<sub>2</sub> than Co. Furthermore, the chronopotentiometry test (CP at a constant 10 mA cm<sup>-2</sup>) was performed for Co/SmH<sub>2</sub>@FTO, Co@FTO, and Pt/C@FTO, and the results are shown in Figure 3d. Evidently, Co/SmH<sub>2</sub>@FTO displayed high stability without any activity decay, which was much higher than those of Co@FTO and Pt/C@FTO, further verifying the crucial role of SmH<sub>2</sub> in stabilizing the activity. Note that, because SmCo<sub>5</sub> exhibits permanent magnetic properties, we deposited it onto FTO (SmCo<sub>5</sub>/FTO) with the same mass loading by using Nafion binder instead of EPD for HER. As

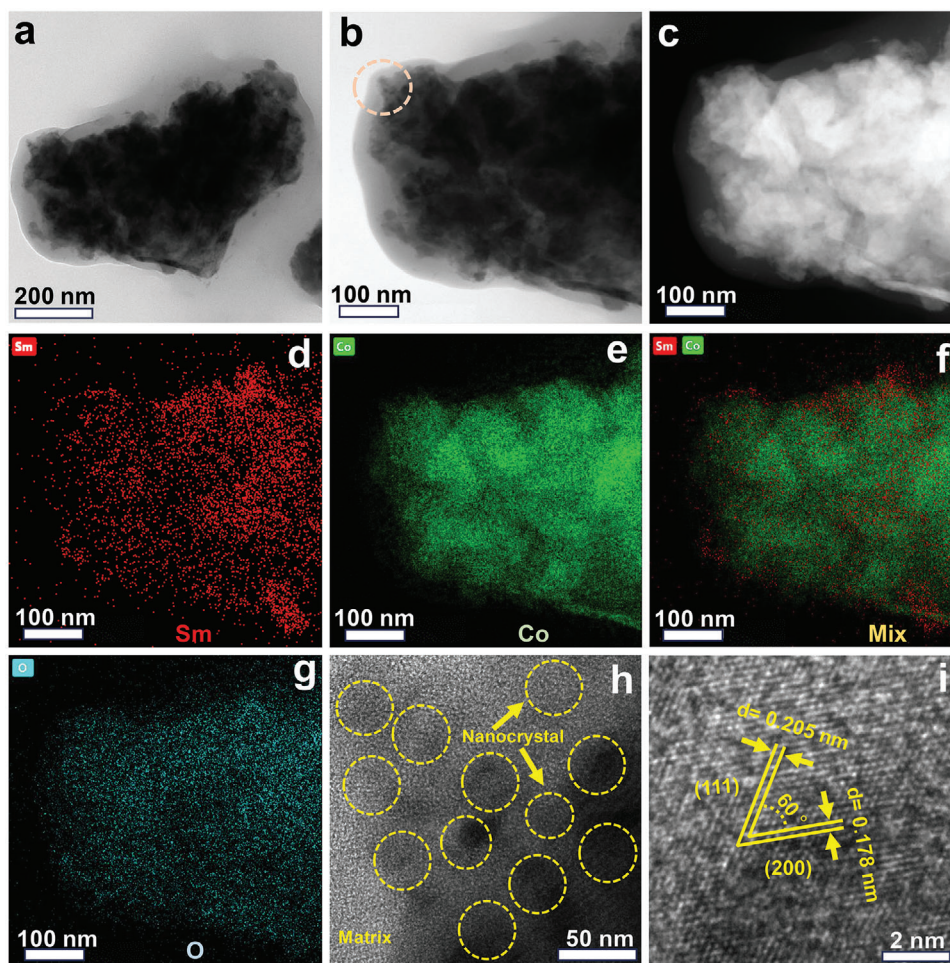


**Figure 4.** a,b) TEM images and c) HAADF image of representative post-HER  $\text{SmH}_2/\text{Co}$  particle and the corresponding EDX elemental mapping of d) Sm, e) Co, and f) their mixture as well as g) O. h) magnified TEM and i) HRTEM images recorded for material in Figure 4a.

shown in Figure S15 (Supporting Information), it delivered an overpotential of 401 mV at  $10 \text{ mA cm}^{-2}$ .

In order to unveil the origin responsible for the superior catalytic activity of  $\text{Co}/\text{SmH}_2@\text{FTO}$ , the electrodes after the CP test were systematically characterized by XRD, XPS, ICP, FE-SEM, and TEM. The XRD results revealed that the phase composition remained essentially unaltered after alkaline HER CA, that is, in addition to the diffraction peaks corresponding to FTO (i.e.,  $\text{SnO}_2$  phase), only peaks associated with  $\text{SmH}_2$  and Co were observed, implying a surface-oriented phase transition (Figure S16, Supporting Information). Further FESEM results suggested observations highlighted a notably roughened surface, with more wrinkled sheets (Figure S17, Supporting Information), confirming the occurrence of surface reconstruction. Interestingly, the surface of pristine Co nanoparticles after HER CA displayed enormous ultrathin sheets, likely resulting from  $\text{OH}^-$  etching on the particle surface (Figure S18, Supporting Information). Low-magnification TEM images of the post-HER  $\text{Co}/\text{SmH}_2@\text{FTO}$  revealed a particle morphology similar to the fresh state (Figure 4a). However, in contrast to the pristine condition, the edge of the particle exhibited a less defined crystalline structure (Figure 4b). To further support this point, The

SAED pattern focused on the edge displayed a distinct halo with a weak diffraction ring, alongside the maintenance of metallic Co phases, suggesting an amorphous feature (Figure S19, Supporting Information). To elucidate the composition differences between the edge and center, HAADF-STEM (Figure 4c) images and corresponding elemental mapping results were provided, which indicated the uniform confinement of Co species by Sm species, with the edge predominantly featuring Sm species rather than Co species (Figure 4c–g). Further, a magnified TEM image revealed the homogeneous distribution of numerous nanocrystals within the particles (Figure 4h), and HRTEM images demonstrated that these nanocrystals were primarily composed of Co phases (Figure 4i). This observation suggested the conversion of surface  $\text{SmH}_2$  into a dominant state of amorphous samarium (hydr)oxide phases. The XPS characterization of the surface post HER CA indicated that there was basically an increase in oxidation state for both Co and Sm species (indicating oxidation of Co due to exposure of cycled sample with a fresh active surface to air and/or electrolyte; Figure S20, Supporting Information). Elemental composition results showed a very small decrease in Sm species after HER (Table S2, Supporting Information), implying the slight dissolution of surface Sm species during

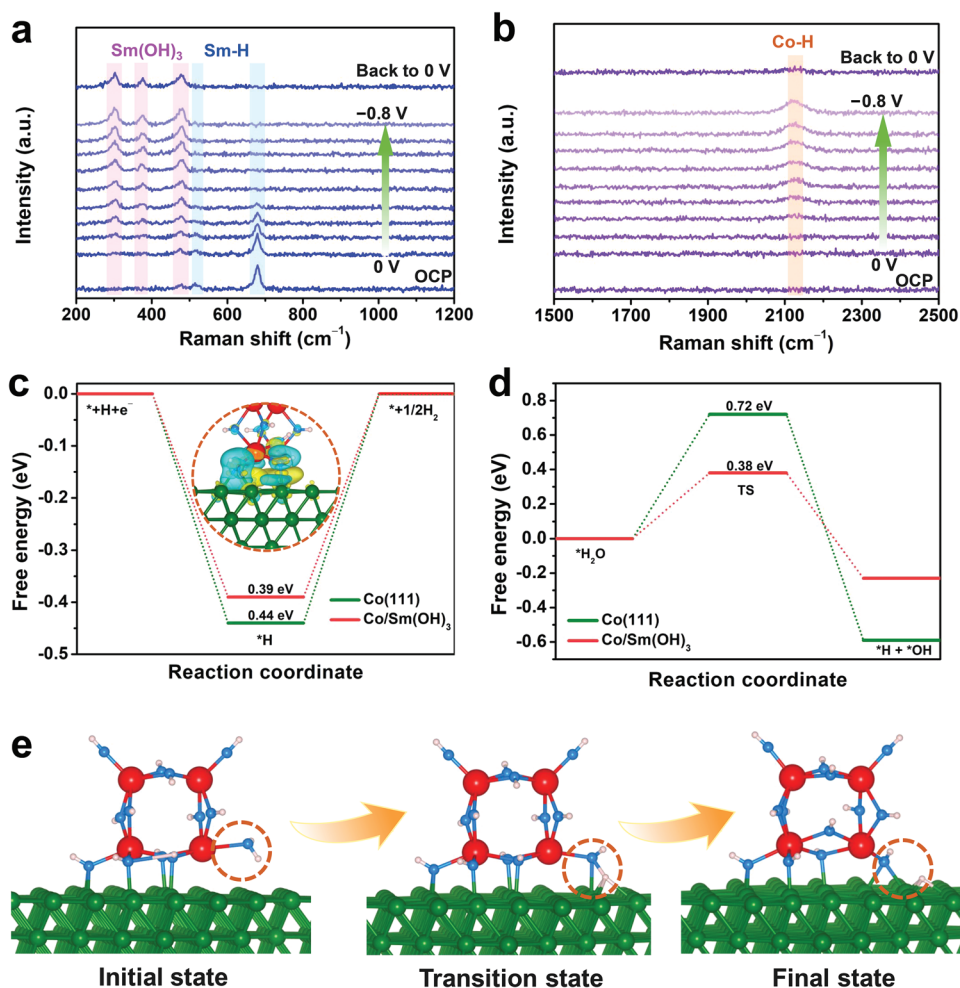


**Figure 5.** In situ Raman spectra of the Co/SmH<sub>2</sub> electrocatalyst recorded within a wavenumber range from a) 200 to 1200 cm<sup>-1</sup> and b) 1500 to 2500 cm<sup>-1</sup> in N<sub>2</sub>-saturated 1 M KOH, spanning a voltage window of 0.0 to -0.8 V versus RHE. Additionally, the Raman spectra are presented in the reverse direction after the forward test from 0.0 to -0.8 V versus RHE. c) Free energy diagram for 2e<sup>-</sup> HER on Co(111) and Co(111)/Sm(OH)<sub>3</sub> at U = 0 V. d) Kinetic barrier of water dissociation on Co(111) and Co(111)/Sm(OH)<sub>3</sub>. e) Atomic configuration of simulated water dissociation process on the calculated Co(111)/Sm(OH)<sub>3</sub>. Inset in (c): differential charge density distribution between Co(111) slab and Sm(OH)<sub>3</sub> cluster, where the green, red, blue, and pink spheres represent the Co, Sm, O, and H atom, respectively, while the yellow and blue color isosurface means the positive and negative charge, respectively.

reconstruction, which might contribute to generating the rough or porous surface for mass transfer. Thus, the above results indicated that Co/SmH<sub>2</sub> serves as a precatalyst for HER, where surface SmH<sub>2</sub> undergoes a transformation into samarium (hydroxide). This transformation continues to confine Co, tuning the catalytic activity and stability. It is noteworthy that the core part retains the Co/SmH<sub>2</sub>, establishing a core-shell architecture after electrochemical reconstruction, ensuring better conductivity for catalysis.

To gain a profound insight into the catalytic dynamics of Co/SmH<sub>2</sub> during the alkaline HER, we employed in situ Raman spectroscopy for detailed characterization. **Figure 5a** presents the in situ Raman spectra covering a band range from 200 to 1500 cm<sup>-1</sup>. The spectra revealed that the signals at 515 and 680 cm<sup>-1</sup> and for the fresh Co/SmH<sub>2</sub>, could be attributed to the Sm-H bond, while the minor peak located at 475 cm<sup>-1</sup> was assigned to the Sm-O bond, likely a consequence of exposure to air.<sup>[47,48]</sup>

Upon applying an HER potential to 0.1 V versus RHE, two new small peaks positioned at ≈303 and 375 cm<sup>-1</sup> emerged, which gradually intensified with the peak positioned at 477 cm<sup>-1</sup>. This indicated the formation of Sm(OH)<sub>3</sub> during the HER process.<sup>[49]</sup> Especially, the peaks located at 303 and 375 cm<sup>-1</sup> were assigned to the translational modes of Sm(OH)<sub>3</sub>, while the band at 477 cm<sup>-1</sup> was designated as the librational model of Sm(OH)<sub>3</sub>.<sup>[49]</sup> Even upon reverting the potential to 0 V versus RHE, these three peaks maintained their high intensity, indicating an irreversible phase transition from SmH<sub>2</sub> to Sm(OH)<sub>3</sub>. On the other hand, **Figure 5b** displayed the in situ Raman spectra across a band range from 1500 to 3000 cm<sup>-1</sup>. As shown in **Figure 5b**, as the applied HER potential reached -0.2 V versus RHE, a new peak appeared at ≈2129 cm<sup>-1</sup>, which could correspond to the Co-H bond.<sup>[50]</sup> Notably, the intensity of this peak gradually increased with rising potential. Upon reverting the potential to 0 V versus RHE, the peak signal weakened significantly, suggesting its catalytic site

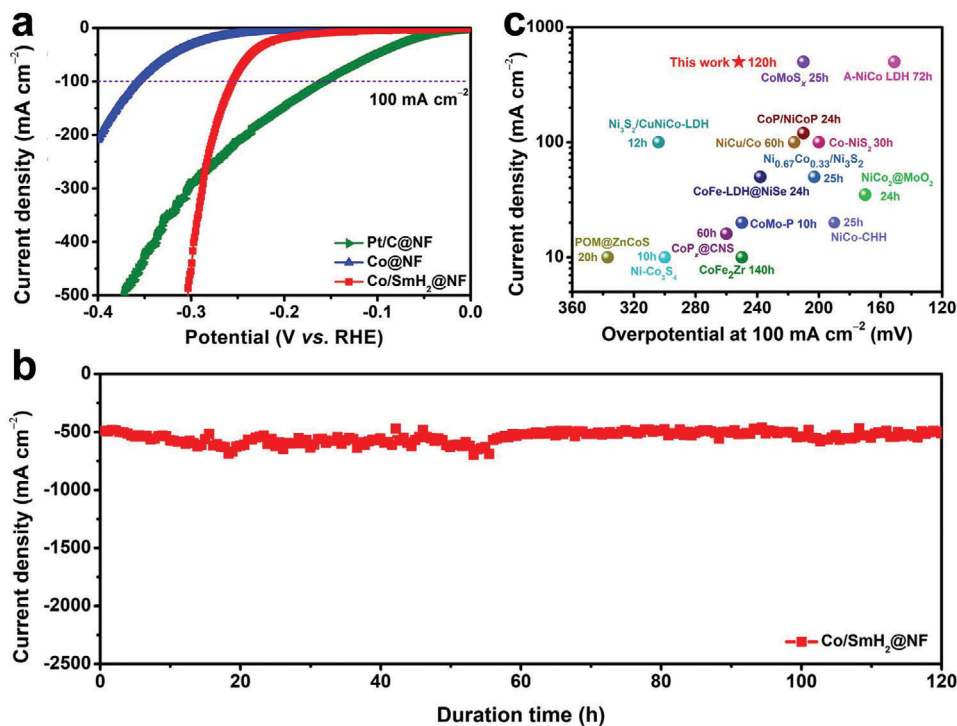


**Figure 6.** a) LSV curves of Co/SmH<sub>2</sub>, Co, Pt/C supported on NF in 1.0 M KOH, b) CA test curve by using Co/SmH<sub>2</sub>@NF as both cathodic and anodic electrode in 1.0 M KOH at an applied potential of 2.11 V, c) Comparison of alkaline HER performance between Co/SmH<sub>2</sub>@NF and recently reported NF-supported Co-based electrocatalysts,<sup>[55–69]</sup> more details can be seen in Table S7 (Supporting Information).

nature. On the other hand, the quasi in situ XAS spectra at the Co K-edge and Sm L<sub>3</sub>-edge in Co/SmH<sub>2</sub>@FTO before and after the HER CP test shown in Figures S21 and S22 (Supporting Information) (simulation results summarized in Tables S5 and S6, Supporting Information) reveal that the metallic Co phase was basically maintained after HER CP while Sm species were largely transformed to hydr(oxide) after HER CP. The obtained results are consistent with the ex situ characterization results for post-HER Co/SmH<sub>2</sub>.

In order to further decouple the mechanism of samarium (hydr)oxide for the improved intrinsic catalytic activity of Co, density functional theory (DFT) calculations were performed to compare the catalytic behavior of Co/Sm(OH)<sub>3</sub> with that of pristine Co. Notably, since rare earth oxides have been demonstrated to be beneficial for the HER activity of transition metal, the role of rare earth metal hydroxide was discussed in this work. First, the structural models of Co (111) and Co(111)/Sm(OH)<sub>3</sub> were constructed based on observed facets from HRTEM. Given the predominantly amorphous nature of Sm(OH)<sub>3</sub>, a corresponding cluster model was rationally devised to simulate the phase structure.<sup>[51,52]</sup> The free adsorption energy of H\* ( $\Delta G_{H^*}$ ) is the critical indicator to estimate the alkaline HER activity of electrocatalysts.<sup>[16]</sup> An ideal HER electrocatalyst should bear moderate free adsorption energy toward H\* ( $\Delta G_{H^*}$ ), which means that the binding ability of the active site to the H atom should be neither too strong nor too weak. Prior to the calculation of  $\Delta G_{H^*}$ , the differential charge density for the Co/Sm(OH)<sub>3</sub> interface was calculated and presented in the inset of Figure 5c, from which the accumulated charge density was clearly observed. This implied synergistic in-

teractions between Co and Sm(OH)<sub>3</sub>, being beneficial for electron transfer. Figure 5c compares the  $\Delta G_{H^*}$  values for Co(111)-H and Co(111)/Sm(OH)<sub>3</sub>-H systems with the most energetically stable configurations (Figure S23, Supporting Information). In terms of Co, the  $\Delta G_{H^*}$  was calculated to be -0.44 eV. This indicated the strong binding ability of H on these sites, resulting in the difficult desorption of H from active sites and unsatisfactory HER performance. As expected, coupling of Co with Sm(OH)<sub>3</sub> could optimize the  $\Delta G_{H^*}$  of Co (-0.39 eV), which would favor the conversion of H\* to H<sub>2</sub>. The d-band center of the interfacial Co atom in Co/Sm(OH)<sub>3</sub> (Figure S24, Supporting Information) negative shift, leading to reduced adsorption energy of Co toward H\*. Furthermore, the energy barrier for water dissociation is another crucial indicator to evaluate the intrinsic catalytic activity for alkaline HER, which was calculated for both the pure Co surface and the Co/Sm(OH)<sub>3</sub> interface (Figure 5d). The energy barrier for water dissociation on the Co(111) surface was calculated as large as 0.72 eV, indicating sluggish water dissociation (Figure 5d). However, the energy barrier for water dissociation could be remarkably lowered to 0.38 eV on the interface of Co(111)/Sm(OH)<sub>3</sub> (Figure 5d), suggesting that the coupling of Sm(OH)<sub>3</sub> could effectively expedite the water dissociation step on Co, being in good agreement with the Tafel slope and EIS findings. This reduced energy barrier was even comparable to that of Pt surface (0.56 eV),<sup>[53]</sup> demonstrating that the incorporated Sm(OH)<sub>3</sub> was an effective promoter for water dissociation. This also assured the adsorption of sufficient hydrogen protons onto the active Co sites of the Co(111)/Sm(OH)<sub>3</sub> interface, facilitating the subsequent Tafel or Heyrovsky process. As depicted in

Figure S25 (Supporting Information), the oxygen atom in the water molecule was adsorbed on the Co site, initiating cleavage into a hydrogen proton and hydroxyl ligand, both adsorbed on the Co site. In contrast, for the Co(111)/Sm(OH)<sub>3</sub> interface, the oxygen atom of water was absorbed on the Sm site of Sm(OH)<sub>3</sub>. Subsequently, the water molecule cleaved into a proton and hydroxyl ligand, adsorbed by Co and the surrounding Sm atom, respectively (Figure 5e). This dual effect of lowering the dissociation energy barrier for water molecules and optimizing  $\Delta G_{H^*}$  highlights the synergistic enhancement of HER kinetics in an alkaline medium, as experimentally confirmed.

Stimulated by promising outcomes, we further deposited the material on NF (Figures S26 and S27, Supporting Information) and evaluated its alkaline HER performance. The LSV results showed an impressive overpotential at 100 mA cm<sup>-2</sup> was only 252 mV (Figure 6a), in addition, the material could maintain a current density of ~500 mA cm<sup>-2</sup> for 120 h with little performance degradation (Figure 6b). The alkaline HER performance at such a large current density was close to that of Pt/C and exceeded those of most currently reported NF-supported Co-based electrocatalysts (Figure 6c). The morphology after cycling indicated a similar structural feature as compared to the fresh one (Figure S28, Supporting Information).

### 3. Conclusion

In summary, we have successfully addressed the research questions (i)–(iv) as mentioned above in the introduction. With respect to question (i), an innovative gaseous engineering strategy was proposed to induce the phase disproportionation of SmCo<sub>5</sub> to enable the in situ confinement of SmH<sub>2</sub> nanocrystals toward Co nanocrystals. To answer questions (ii)–(iv), the as-prepared Co/SmH<sub>2</sub> was electrophoretically deposited on FTO and explored for the alkaline HER for the first time. Further ex situ and in situ spectra characterization and results from DFT calculation uncovered that the Co/SmH<sub>2</sub> acts as a precatalyst, in which surface SmH<sub>2</sub> was transformed to the samarium (hydr)oxide during alkaline HER that further uniformly confined and tuned the coupled SmH<sub>2</sub>. This in situ coupling mechanism not only curtailed the aggregation of Co nanocrystals, ensuring high structural stability but also reduced the energy barrier for water dissociation while optimizing free adsorption energy toward H, greatly enhancing the intrinsic reaction kinetics and thermodynamics. Furthermore, the unconverted inner Co/SmH<sub>2</sub> part ensured better electron transport during HER. After a thorough intrinsic HER activity measurement of Co/SmH<sub>2</sub> on FTO, it was deposited on nickel foam, which demonstrated an excellent overpotential of 252 mV at 100 mA cm<sup>-2</sup> and sustained stability at 500 mA cm<sup>-2</sup> for 120 h. This alkaline HER performance surpassed the majority of previously reported transition metal-based electrocatalysts. This study not only introduces a novel design concept for cost-effective, stable, and efficient earth-abundant rare earth-transition metal-based electrocatalysts but also provides profound fundamental insights into the correlation among composition-structure-activity. Furthermore, to the best of our knowledge, this is the first case to show the hydrogen-induced disproportionation of intermetallics for enhancing the hydrogen evolution activity of transition metals. Actually, owing to the high binding energy of rare earth to hydrogen, many rare earth-

transition metal based intermetallics, especially for the AB<sub>x</sub>-type intermetallics (A = rare earth metal, B = transition metal,  $x = 2, 3, 3.5, 4, 5$ ) can be converted into the composite composed of rare earth hydrides and transition metals by gaseous hydrogenation. Notably, surface oxidation can occur for many rare earth metal hydrides under air, but this will hardly affect the surface catalytic behavior of the designed composite as these surface hydrides would be eventually converted to rare earth (hydr) oxides after alkaline catalysis. This encouraging work is expected to trigger more interesting investigations in the future.

### Supporting Information

Supporting Information is available from the Wiley Online Library or from the author.

### Acknowledgements

This work is supported by National Natural Science Foundation of China (52201269), Natural Science Foundation of Jiangsu Province (BK20210735), Collaborative Innovation Center of Suzhou Nano Science & Technology, the 111 Project, and Suzhou Key Laboratory of Functional Nano & Soft Materials and Jiangsu Key Laboratory for Advanced Negative Carbon Technologies. The authors thank the Helmholtz-Zentrum Berlin (HZB) for beamtime allocation at the KMC-3 synchrotron beamline of the BESSY synchrotron in Berlin-Adlershof and Dr. Ivo Zizak for technical support. Z.C. gratefully acknowledges the funding from Gusu leading talent plan for scientific and technological innovation and entrepreneurship (ZXL2022487). H. Yang thanks China Scholarship Council (CSC) for the Ph.D. fellowship. P. W. Menezes greatly acknowledges support from the German Federal Ministry of Education and Research in the framework of the project Catlab (03EW0015A/B) and PrometH2eus (03HY105C). I. M. thanks SERB Ramanujan Fellowship. M.D. thanks the Deutsche Forschungsgemeinschaft (Germany's Excellence Strategy – EXC 2008/1-390540038 – UniSysCat) for financial support.

Open access funding enabled and organized by Projekt DEAL.

### Conflict of Interest

The authors declare no conflict of interest.

### Data Availability Statement

The data that support the findings of this study are available from the corresponding author upon reasonable request.

### Keywords

alkaline hydrogen evolution, disproportionation, gaseous hydrogen engineering, phase reconstruction, rare earth-transition metal intermetallics

Received: February 13, 2024  
Revised: March 12, 2024  
Published online: April 9, 2024

- [1] S. Carley, D. M. Konisky, *Nat. Energy* **2020**, *5*, 569.  
[2] Z. Yu, Y. Duan, X. Feng, X. Yu, M. Gao, S. Yu, *Adv. Mater.* **2021**, *33*, 2007100.

- [3] Z. Chen, H. Yang, Z. Kang, M. Driess, P. W. Menezes, *Adv. Mater.* **2022**, *34*, 2108432.
- [4] Y. Shi, Z. Ma, Y. Xiao, Y. Yin, W. Huang, Z. Huang, Y. Zheng, F. Mu, R. Huang, G. Shi, Y. Sun, X. Xia, W. Chen, *Nat. Commun.* **2021**, *12*, 3021.
- [5] C. Panda, P. W. Menezes, M. Driess, *Angew. Chem., Int. Ed.* **2018**, *57*, 11130.
- [6] T. Tang, L. Ding, Z. Yao, H. Pan, J. Hu, L. Wan, *Adv. Funct. Mater.* **2022**, *32*, 2107479.
- [7] T. Kou, M. Chen, F. Wu, T. J. Smart, S. Wang, Y. Wu, Y. Zhang, S. Li, S. Lall, Z. Zhang, Y. Liu, J. Guo, G. Wang, Y. Ping, Y. Li, *Nat. Commun.* **2020**, *11*, 590.
- [8] S. Anantharaj, S. Noda, V. R. Jothi, S. Yi, M. Driess, P. W. Menezes, *Angew. Chem., Int. Ed.* **2021**, *60*, 18981.
- [9] K. Dastafkan, X. Shen, R. K. Hocking, Q. Meyer, C. Zhao, *Nat. Commun.* **2023**, *14*, 547.
- [10] X. F. Lu, S. L. Zhang, W. L. Sim, S. Y. Gao, X. W. Lou, *Angew. Chem., Int. Ed.* **2021**, *60*, 22885.
- [11] L. M. Wang, L. L. Zhang, W. Ma, H. Wan, X. J. Zhang, X. Zhang, S. Y. Jiang, J. Y. Zheng, Z. Zhou, *Adv. Funct. Mater.* **2022**, *32*, 2203342.
- [12] W. Xu, G. Fan, S. Zhu, Y. Liang, Z. Cui, Z. Li, H. Jiang, S. Wu, F. Cheng, *Adv. Funct. Mater.* **2021**, *31*, 2107333.
- [13] S. Anantharaj, S. R. Ede, K. Sakthikumar, K. Karthick, S. Mishra, S. Kundu, *ACS Catal.* **2016**, *6*, 8069.
- [14] C. Panda, P. W. Menezes, S. Yao, J. Schmidt, C. Walter, J. N. Hausmann, M. Driess, *J. Am. Chem. Soc.* **2019**, *141*, 13306.
- [15] M. Gong, D. Wang, C. Chen, B. Hwang, H. Dai, *Nano Res.* **2016**, *9*, 28.
- [16] K. Xu, H. Cheng, H. Lv, J. Wang, L. Liu, S. Liu, X. Wu, W. Chu, C. Wu, Y. Xie, *Adv. Mater.* **2018**, *30*, 1703322.
- [17] C. Panda, P. W. Menezes, M. Zheng, S. Orthmann, M. Driess, *ACS Energy Lett.* **2019**, *4*, 747.
- [18] X. R. Sun, S. B. Wang, Y. D. Hou, X. F. Lu, J. J. Zhang, X. C. Wang, *J. Mater. Chem. A* **2023**, *11*, 13089.
- [19] P. Wang, K. Wang, Y. J. Liu, H. F. Li, Y. Guo, Y. Tian, S. Guo, M. C. Luo, Y. He, Z. M. Liu, S. J. Guo, *Adv. Funct. Mater.* **2024**, 2316709.
- [20] L. Zhao, Y. Zhang, Z. Zhao, Q. Zhang, L. Huang, L. Gu, G. Lu, J. Hu, L. Wan, *Natl. Sci. Rev.* **2020**, *7*, 27.
- [21] Y. Li, X. Tan, R. K. Hocking, X. Bo, H. Ren, B. Johannessen, S. C. Smith, C. Zhao, *Nat. Commun.* **2020**, *11*, 2720.
- [22] D. S. Hall, C. Bock, B. R. MacDougall, *J. Electrochem. Soc.* **2013**, *160*, F235.
- [23] I. T. McCrum, M. T. M. Koper, *Nat. Energy* **2020**, *5*, 891.
- [24] C. Wan, Z. Zhang, J. Dong, M. Xu, H. Pu, D. Baumann, Z. Lin, S. Wang, J. Huang, A. H. Shah, X. Pan, T. Hu, A. N. Alexandrova, Y. Huang, X. Duan, *Nat. Mater.* **2023**, *22*, 1022.
- [25] M. Gong, W. Zhou, M. Tsai, J. Zhou, M. Guan, M. Lin, B. Zhang, Y. Hu, D. Wang, J. Yang, S. J. Pennycook, B. Hwang, H. Dai, *Nat. Commun.* **2014**, *5*, 4695.
- [26] L. Dai, Z. Chen, L. Li, P. Yin, Z. Liu, H. Zhang, *Adv. Mater.* **2020**, *32*, 1906915.
- [27] Y. Luo, X. Li, X. Cai, X. Zou, F. Kang, H. Cheng, B. Liu, *ACS Nano* **2018**, *12*, 4565.
- [28] S. Xue, R. W. Haid, R. M. Kluge, X. Ding, B. Garlyyev, J. Fichtner, S. Watzel, S. Hou, A. S. Bandarenka, *Angew. Chem., Int. Ed.* **2020**, *59*, 10934.
- [29] R. Subbaraman, D. Tripkovic, D. Strmcnik, K. Chang, M. Uchimura, A. P. Paulikas, V. Stamenkovic, N. M. Markovic, *Science* **2011**, *334*, 1256.
- [30] X. Chen, J. Wan, J. Wang, Q. Zhang, L. Gu, L. Zheng, N. Wang, R. Yu, *Adv. Mater.* **2021**, *33*, 2104764.
- [31] M. Luo, J. Yang, X. Li, M. Eguchi, Y. Yamauchi, Z. Wang, *Chem. Sci.* **2023**, *14*, 3400.
- [32] J. Huang, J. Han, T. Wu, K. Feng, T. Yao, X. Wang, S. Liu, J. Zhong, Z. Zhang, Y. Zhang, B. Song, *ACS Energy Lett.* **2019**, *4*, 3002.
- [33] H. Sun, Z. Yan, C. Tian, C. Li, X. Feng, R. Huang, Y. Lan, J. Chen, C. Li, Z. Zhang, M. Du, *Nat. Commun.* **2022**, *13*, 3857.
- [34] K. Wu, L. D. Sun, C. H. Yan, *Adv. Energy Mater.* **2016**, *6*, 1600501.
- [35] Z. Chen, H. Yang, S. Mebs, H. Dau, M. Driess, Z. Wang, Z. Kang, P. W. Menezes, *Adv. Mater.* **2023**, *35*, 2208337.
- [36] X. Guo, S. Wang, X. Liu, Z. Li, J. Ye, H. Yuan, L. Jiang, *Int. J. Miner. Metall. Mater.* **2012**, *19*, 1010.
- [37] D. Sun, F. Gingl, Y. Nakamura, H. Enoki, M. Bououdina, E. Akiba, *J. Alloys Compd.* **2002**, *333*, 103.
- [38] G. K. Schweitzer, L. L. Pesterfield, *The Aqueous Chemistry of the Elements*, OUP USA, New York, **2010**.
- [39] I. I. Bulyk, A. M. Trostyanchyn, V. I. Markovych, *Mater. Sci.* **2007**, *43*, 102.
- [40] J. W. Larsen, B. R. Livesay, *J. Less Common Met.* **1980**, *73*, 79.
- [41] A. Longo, L. Sciortino, F. Giannicci, A. Martorana, *J. Appl. Crystallogr.* **2014**, *47*, 1562.
- [42] G. Cheng, J. D. Carter, T. Guo, *Chem. Phys. Lett.* **2004**, *400*, 122.
- [43] M. Manjum, N. Serizawa, A. Ispas, A. Bund, Y. Katayama, *J. Electrochem. Soc.* **2020**, *167*, 042505.
- [44] I. Mondal, J. N. Hausmann, G. Vijaykumar, S. Mebs, H. Dau, M. Driess, P. W. Menezes, *Adv. Energy Mater.* **2022**, *12*, 2200269.
- [45] H. Shi, Y. Zhou, R. Yao, W. Wan, X. Ge, W. Zhang, Z. Wen, X. Lang, W. Zheng, Q. Jiang, *Nat. Commun.* **2020**, *11*, 2940.
- [46] H. Meng, M. A. Kuzovnikov, M. Tkacz, *Int. J. Hydrog. Energy* **2017**, *42*, 29344.
- [47] S. Jiang, J. Liu, C. Lin, X. Li, Y. Li, *J. Appl. Phys.* **2013**, *113*, 113502.
- [48] S. R. Shieh, T. S. Duffy, *Phys. Rev. B* **2002**, *66*, 134301.
- [49] Q. Mu, Y. Wang, *J. Alloys Compd.* **2011**, *509*, 2060.
- [50] M. Wang, K. Sun, W. Mi, C. Feng, Z. Guan, Y. Liu, Y. Pan, *ACS Catal.* **2022**, *12*, 10771.
- [51] J. Wu, M. Hou, Z. Chen, W. Hao, X. Pan, H. Yang, W. Cen, Y. Liu, H. Huang, P. W. Menezes, Z. Kang, *Adv. Mater.* **2022**, *34*, 2202995.
- [52] J. O. Juárez-Sánchez, D. H. Galván, A. Posada-Amarillas, *Comput. Theor. Chem.* **2017**, *1103*, 71.
- [53] K. Jiang, B. Liu, M. Luo, S. Ning, M. Peng, Y. Zhao, Y. Lu, T. Chan, F. M. F. de Groot, Y. Tan, *Nat. Commun.* **2019**, *10*, 1743.
- [54] P. W. Menezes, C. Panda, C. Walter, M. Schwarze, M. Driess, *Adv. Funct. Mater.* **2019**, *29*, 1808632.
- [55] W. Lu, X. Li, F. Wei, K. Cheng, W. Li, Y. Zhou, W. Zheng, L. Pan, G. Zhang, *Electrochim. Acta* **2019**, *318*, 252.
- [56] Y. Han, P. Li, Z. Tian, C. Zhang, Y. Ye, X. Zhu, C. Liang, *ACS Appl. Energy Mater.* **2019**, *2*, 6302.
- [57] H. Yang, Z. Chen, P. Guo, B. Fei, R. Wu, *Appl. Catal. B, Environ.* **2020**, *267*, 118240.
- [58] L. Huang, D. Chen, G. Luo, Y. Lu, C. Chen, Y. Zou, C. Dong, Y. Li, S. Wang, *Adv. Mater.* **2019**, *31*, 1901439.
- [59] S. M. N. Jeghan, D. Kim, Y. Lee, M. Kim, G. Lee, *Appl. Catal. B, Environ.* **2022**, *308*, 121221.
- [60] X. Shan, J. Liu, H. Mu, Y. Xiao, B. Mei, W. Liu, G. Lin, Z. Jiang, L. Wen, L. Jiang, *Angew. Chem., Int. Ed.* **2020**, *59*, 1659.
- [61] C. Hou, L. Zou, Y. Wang, Q. Xu, *Angew. Chem., Int. Ed.* **2020**, *59*, 21360.
- [62] Y. Lin, K. Sun, S. Liu, X. Chen, Y. Cheng, W. Cheong, Z. Chen, L. Zheng, J. Zhang, X. Li, Y. Pan, C. Chen, *Adv. Energy Mater.* **2019**, *9*, 1901213.
- [63] J. Gautam, Y. Liu, J. Gu, Z. Ma, J. Zha, B. Dahal, L. Zhang, A. N. Chishti, L. Ni, G. Diao, Y. Wei, *Adv. Funct. Mater.* **2021**, *31*, 2106147.
- [64] Z. Wu, Y. Feng, Z. Qin, X. Han, X. Zheng, Y. Deng, W. Hu, *Small* **2022**, *18*, 2106904.
- [65] L. Jia, G. Du, D. Han, Y. Hao, W. Zhao, Y. Fan, Q. Su, S. Ding, B. Xu, *J. Mater. Chem. A* **2021**, *9*, 27639.

- [66] A. Kumar, S. K. Purkayastha, A. K. Guha, M. R. Das, S. Deka, *ACS Catal.* **2023**, *13*, 10615.
- [67] J. Wu, J. Chen, T. Yu, Z. Zhai, Y. Zhu, X. Wu, S. Yin, *ACS Catal.* **2023**, *13*, 13257.
- [68] J. Yin, J. Jin, H. Zhang, M. Lu, Y. Peng, B. Huang, P. Xi, C. Yan, *Angew. Chem., Int. Ed.* **2019**, *58*, 18676.
- [69] S. Tang, X. Wang, Y. Zhang, M. Courté, H. Fan, D. Fichou, *Nanoscale* **2019**, *11*, 2202.